Characterization of Porosity and Pore Accessibility of Vitrinite-Rich Bituminous and Subbituminous Coals by Small Angle Neutron Scattering, Mercury Intrusion Porosimetry, and Low Pressure N_2 Adsorption

Ercan Cakmak[a*], Aparna Annamraju[b], Jonathan P. Mathews[c], Lilin He[d], Nidia Gallego[b] and Edgar Lara-Curzio[a]

[a] *Materials Science and Technology Division, Oak Ridge National Laboratory, Oak Ridge, TN 37831, USA*

[b] *Chemical Sciences Division, Oak Ridge National Laboratory, Oak Ridge, TN 37831, USA*

[c] *Leone Family Department of Energy and Mineral Engineering, and the EMS Energy Institute, The Pennsylvania State University, USA*

[d] *Neutron Scattering Division, Oak Ridge National Laboratory, Oak Ridge, TN 37831, USA*

***Corresponding Author:**

Ercan Cakmak

Materials Science and Technology Division

Oak Ridge National Laboratory[#]

Oak Ridge, TN 37831-6064

Tel: (865) 574-6538

E-mail: cakmake@ornl.gov

[*] Author to whom correspondence should be addressed; electronic mail: cakmake@ornl.gov

---

[#] This manuscript has been authored by UT-Battelle, LLC under Contract No. DE-AC05-00OR22725 with the U.S. Department of Energy. The United States Government retains and the publisher, by accepting the article for publication, acknowledges that the United States Government retains a non-exclusive, paid-up, irrevocable, world-wide license to publish or reproduce the published form of this manuscript, or allow others to do so, for United States Government purposes. The Department of Energy will provide public access to these results of federally sponsored research in accordance with the DOE Public Access Plan (http://energy.gov/downloads/doe-public-access-plan).

Abstract

Three bituminous and one sub-bituminous vitrinite-rich coals were characterized using small angle neutron scattering with contrast matching, mercury intrusion porosimetry and low pressure N_2 adsorption techniques to quantify their porosity and pore accessibility; in an effort to assess their solvent extractabilities, as a first approximation, for manufacturing useful end-products. The techniques revealed consistent results while complimenting one another. The total porosity was found to follow the coal rank with the lowest rank having the highest porosity within the studied coals. The amount of inaccessible pores was found to increase with rank for the bituminous coals studied here. The increase in the ease of accessibility and total porosity with decreasing rank suggested easier penetration of chemical reagents for solvent extraction, for example.

1. Introduction

During the last 10 years, U.S. coal production, consumption, and employment have decreased continuously, and these trends are likely to persist as coal will continue losing market share to cleaner natural gas and renewable energy generation in the electric power sector. However, the abundant coal reserves in the U.S., combined with the presence of critical minerals within coal, and the growing use of carbonaceous materials in a broad set of technologies, provide a unique opportunity for developing new industries that utilize coal feedstocks to produce precursors for manufacturing high value-added products. The idea of using coal as a feedstock for manufacturing products is not new, as illustrated by the many "coal trees" that have been published over the last 100 years [1-8].

Coal is a soft sedimentary rock composed of a complex organic matrix intertwined with inorganic components [9-11] along with a complex pore/cleat structure [12, 13]. Furthermore, the pore size distribution spans several length scales, from the seam to the molecular level [14]. Processing coal to produce feedstocks for products requires an understanding of the distribution of pore sizes and how pores interact with various fluids. This chemical and structural heterogeneous nature can make fluid accessibility of the invading gas or liquid a challenge.

Pores in coals are generally classified by width into three main categories: micropores (<20 Å, 2nm), mesopores (20-500 Å, 2-50 nm), and macropores (>500 Å, 50nm) [15]. Coal porosity is a key component of coal utilization for methane extraction, gasification, liquefaction, coke production, etc. [16-18]. Particularly, for chemical reactions requiring a solvent, the pore surface area can be significant with micropores contributing a major portion of the available surface area for bituminous coals [16, 19]. For much of the rank range however, there is a broad range of pore sizes [14] and it is clear that the simplification of dual porosity (cleats and micropores) is limited to selected vitrinite-rich bituminous coals [20]. During coalification, the loss of oxygen as H_2O and CO_2 reduces the water holding capacity and combined with in-situ stress, causes a reduction (compression/collapse) in the macroporosity. Additional light gas production creates open porosity when those gases escape or migrate along with coal shrinkage. Later at a bituminous rank, as gas production continues (increasingly CH_4) the crystal structure further evolves [21] and structural rearrangements may result in further transitions in the pore structure, including closed pores even to small probe molecules (<4Å). Molecule migration from "bitumen" production may also contribute. These compositional and physical changes cause the porosity (as measured by He) to vary considerably by rank [19] as well (as measured by CO_2) as its maceral composition [20, 22].

While the research on crushed coal is of interest here, it is worth mentioning that the situation is more complex in-situ (i.e., in the coal bed) with confining stresses reducing cleat apertures and closing others [23], and compressing the pore structure as shown by reduced gas uptake [24, 25]. Gas uptake can also cause stress-induced fracturing [26] with lithotypes impacting the expansion/compression behavior with gas uptake, i.e., compression of some lithotypes by the other expanding lithotypes [27]. Thus, porosity is a structural part of coals at various length scales and can form a complex network affected by multiple factors during formation/maturation. Accordingly, a detailed characterization of coal porosity and its size distribution is helpful as a first approximation to design processes for using coal as feedstock for manufacturing high value end-products.

Mercury Intrusion Porosimetry (MIP) and N_2 adsorption/desorption measurements are the two most commonly employed techniques to determine coal porosity [28-30]. However, these methods operate on different length-scales, with MIP generally used to quantify meso- and macroporosity, and N_2 adsorption for micro- and mesoporosity [30]. While MIP covers a considerable pore size range for crushed coals, it is the most intrusive as it relies on increasing mercury pressures to access increasingly smaller pores by overcoming capillary resistance [29]. However, because of the low bulk modulus of coal, as the hydrostatic pressure increases the skeletal matrix will deform, thus limiting accurate determination of the contribution of smaller pores (<50 nm) [14, 29]. Although low pressure nitrogen adsorption is not as intrusive as MIP, it only provides information pertaining to open pores at the meso- to micro-porosity scale.

Small angle scattering (SAS) techniques using either X-rays (SAXS) or neutrons (SANS) enables detection of pore size distributions (with a reasonable assumption of the pore shapes) in a homogeneous media of condensed matter and pores with distinct interfaces. Additionally, SAS techniques are non-destructive and can probe wider range of pore size distribution. In SANS closed pores can also be detected with contrast matching fluid or gas sorption, when compared to MIP or N_2 adsorption techniques which often rely on infiltration of the pore network through openings. For coals, SANS is advantageous over SAXS as contrast differences between mineral matter and coal matrix does not affect the scattering measurement [14, 31].

The objective of this paper is to compare the porosity of four different coals consisting of three bituminous and one subbituminous coals. The pore size distribution, porosity, and pore accessibility were investigated using SANS, MIP, and low pressure N_2 adsorption techniques.

The measured porosity data using these techniques are discussed in terms of total porosity, pore size distributions, and pore accessibility to a D_2O/H_2O contrast matching fluid (for SANS). The results are also correlated to coal rank where applicable. These data are fundamental coal physical structural properties and will impact coal behavior particularly in regard to gas storage/extraction, solvent extraction, and liquefaction.

2. Experimental details

2.1. Coal samples

Two bituminous coals from the Illinois Basin (Herrin and Springfield), one from Central Appalachian (Blue Gem), and a subbituminous coal from the Powder River Basin (Monarch) were used in the study. Herrin and Springfield are abundant, accessible coals and were selected due to their similarity to Blue Gem (a much less abundant coal with exceptionally low ash content), while Monarch coal was selected for its subbituminous nature.

The coals were coarse ground and sieved to a size distribution of 0.5-1 mm [22, 23], mainly to avoid scattering from interparticle voids during SANS measurements. Additionally, the use of powders enables an averaging of the macerals from all orientations [14]. The same size range was also used for the MIP measurements to avoid problems stemming from interparticle spacing which can become a significant problem with fine powders [32]. For consistency, the low pressure N_2 adsorption measurements were also performed on the same size range. To allow the fluids/gasses to penetrate into these coarse grains, longer equilibration times were employed compared to finer powder sizes (~0.2 μm) typically used for these methods.

For the SANS, MIP, and low pressure N_2 adsorption measurements the samples were dried overnight under vacuum before the experiments.

2.2. Small angle neutron scattering measurements

The SANS measurements were performed at the GP-SANS beamline of the High Flux Isotope Reactor, Oak Ridge National Laboratory (ORNL) [33]. The coal powder samples were loaded into demountable cells with a thickness of 1mm. Three instrument configurations with $\lambda = 12$ Å ($\Delta\lambda/\lambda = 0.13$) and a sample-to-detector distance (SDD) of 19 m, followed by $\lambda = 4.75$ Å ($\Delta\lambda/\lambda = 0.13$) and SDDs of 7 m and 1 m were chosen to cover the Q range of $6\text{x}10^{-4}$ to 0.8 Å^{-1}. All measurements were conducted at room temperature, and the scattering cross sections were calibrated by a secondary standard and corrected for empty cell scattering, sample transmission, thickness, and detector sensitivity. The azimuthally isotropic two-dimensional (2D) scattering patterns were then reduced to one-dimensional (1D) intensity I as a function of Q using drtsans. Contrast matching measurements [34] were conducted to allow the open pores to be filled with a fluid that has the same scattering length density (SLD) as the matrix. This was achieved using mixtures of D_2O/H_2O (distilled) with the ratio adjusted for each coal. Under the contrast matching condition, only the closed pores (inaccessible to the invading fluid) are detected [35]. For data quantification, the 1D SANS datasets were fitted with a Polydisperse Spherical Particle (PDSP) Model using the PRINSAS software [36].

2.3. Mercury intrusion porosimetry (MIP)

The MIP analysis was conducted on a Micromeritics Autopore V 9620 instrument, using ~1 g of sample and nominal 5 cm^3 powder penetrometers with 0.4 cm^3 stem. The pressure was applied stepwise up to a total pressure of 346 MPa (50.18 ksi). However, for most of the paper, pore size distribution, and pore volume results are reported over the pressure range between 0.2 to 32 MPa, assuming a consistent contact angle of 140° between mercury and the material. This pressure range was selected based on two criteria. First, the upper limit was selected based on data from the literature [30] aiming to optimize the maximum detectable pore size while preserving the soft coal skeletal structure. The lower limit was selected following [37] where the interparticle void filling pressure (P) is calculated per the relation in Eq. (1),

$$P \approx \frac{200\gamma}{\delta} \tag{1}$$

where γ=0.48 Pa.m and δ (m) is the diameter of the spherical particles. For a particle size distribution of 0.5-1 mm, the pressures required to fill the interparticle void space would be 0.1-0.2 MPa.

The pore radii were calculated using the Washburn equation that defines the relation between the applied mercury pressure, P, and the minimum radius, r, of a cylindrical pore that it fills following the relation:

$$P = -2\sigma cos\theta/r \tag{2}$$

where σ is the surface tension of mercury (485 mN/m), and θ is the mercury-solid contact angle [38, 39].

2.4. Low pressure N_2 adsorption

Low pressure N_2 adsorption measurements were conducted on an Autosorb-iQ surface area and porosity analyzer from Quantachrome Instruments (a brand of Anton Paar, Boynton Beach, FL, USA). Prior to adsorption analysis, coal samples (1-2 g) were dried overnight under high vacuum. Data reduction was performed using commercial software ASiQwin 4.0 available from Quantachrome Instruments. Adsorption data were used to calculate the BET surface area (S_{BET}). Adsorption surface area, pore volume and distribution were obtained from Barrett-Joyner-Halenda (BJH) relationship typically used for mesoporous materials and Density Functional Theory model using Quenched Solid Density Functional Theory (QSDFT) for slit pore estimation.

3. Results and Discussion

3.1. Basic properties of coals

As can be seen in Table 1, all the studied coals are vitrinite-rich. Based on their vitrinite reflectance values the coals can be ranked in the following order: Blue Gem, Springfield, Herrin, and Monarch. Basic structural information is presented in Table 1 to aid in further discussions. These include the maceral compositions, vitrinite reflectance values (R_0, max) and He densities. A more detailed structural characterization of these coals will be published in a companion paper [40].

3.2. Porosity results from SANS measurements

Radially symmetric 2D SANS patterns were converted into to 1D data via azimuthal averaging. The absolute neutron scattering intensities, I(Q), are presented in Figure 1a as a function of the scattering vector, Q, for all the coals. The corresponding pore sizes were calculated following the relation: $R \approx 2.5/Q$ [14, 41].

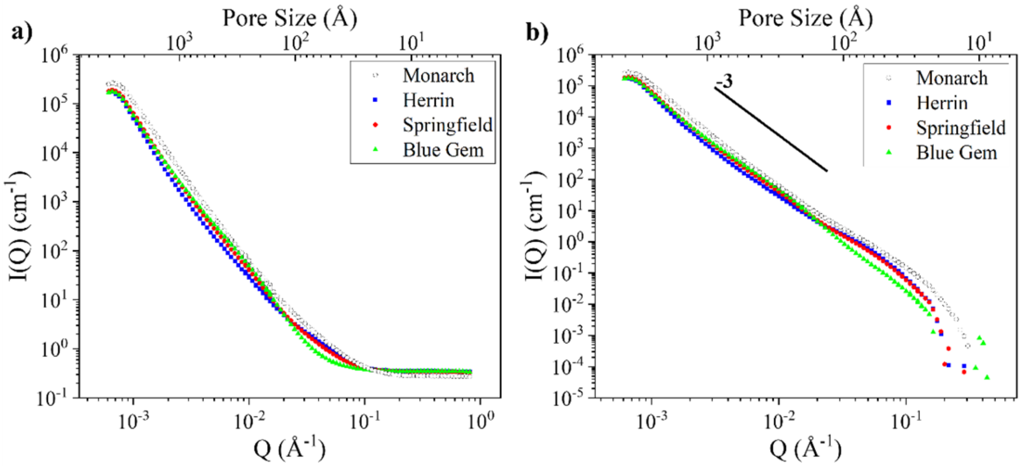

Figure 1. a) Neutron scattering intensities as a function of the scattering vector Q for all four coals. b) Intensities after subtracting the incoherent scattering background from a).

A near-linear relation between the I(Q) and Q values is observed for all the coals in Figure 1a up until a Q value of ~0.06 Å^{-1}. The non-linear portion of the curve where I(Q) vs Q relation becomes flat is ascribed to the incoherent background scattering arising from organic matter, e.g., polyaromatic sheets [14, 42]. For further interpretation of the data, the constant incoherent background is subtracted, and the profiles are shown in Figure 1b. For the background subtraction, we assumed that the interface between the pores and the empty space is smooth and follows Q^{-4} behavior at high Q. It was obtained from the slope of a plot of $Q^4I(Q)$ vs Q^4.

The I(Q) exhibiting a power law decay against Q results from a distribution of spherical pores bounded by surfaces with a fractal dimension [42, 43]. The slope of the linear portion of the I(Q)-Q curve is reported to range between -3 and -4 for surface fractals and between -2 and -3 for mass fractals [14, 44]. While the majority of surface fractals remain in the bulk, mass fractals are accessible from the exterior (e.g., a network of cracks) [44, 45]. The slope values for the linear sections of the SANS data in Figure 1b are as follows; Monarch (-3.02±0.02), Herrin (-

2.98±0.03), Springfield (-3.02±0.02), and Blue Gem (-3.11±0.02). These values indicate surface fractal geometry of the matrix-pore interfaces of the coals. A reference line with a slope of -3 is shown in Figure 1b.

The scattering from surface fractals were fitted with the Polydisperse Spherical Particle (PDSP) Model for further quantification using the PRINSAS software [36] and are shown in Figure 2 as solid lines over experimental data points. Porosity fraction, pore size distribution, and specific surface areas (SSA) are obtained from the fit results.

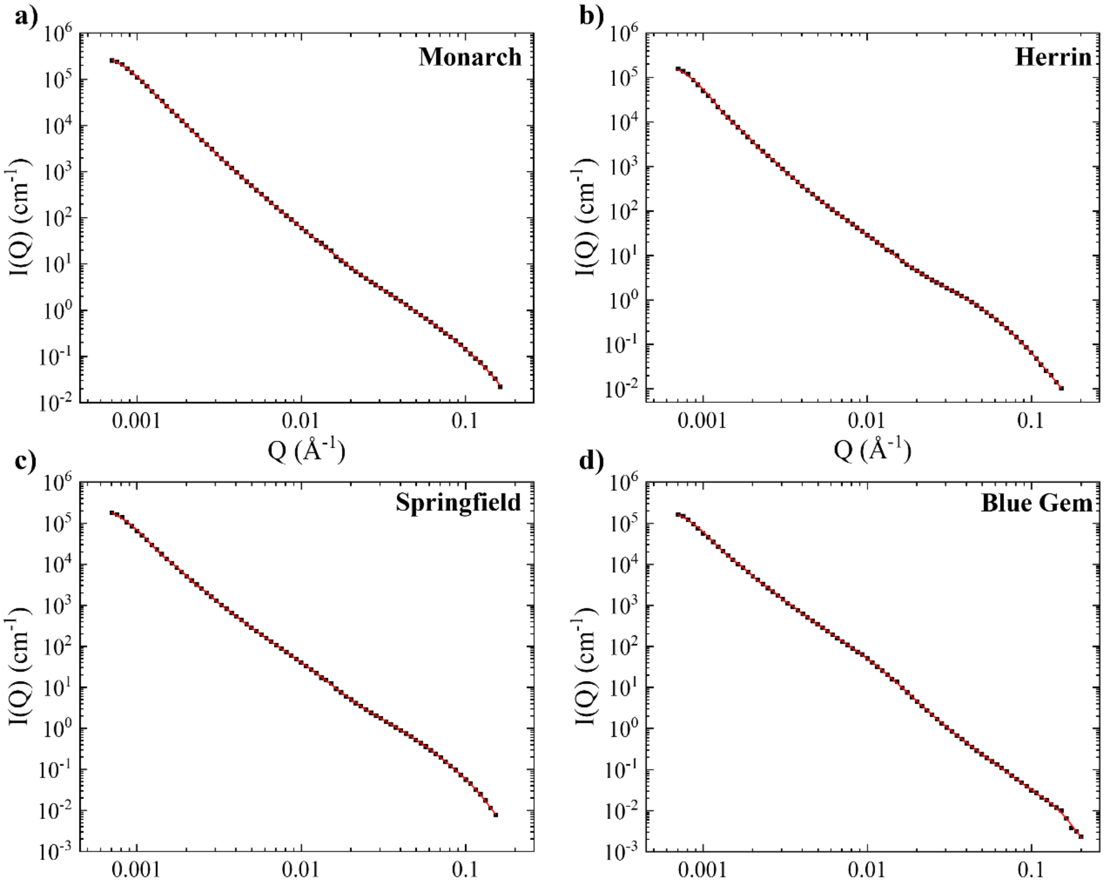

Figure 2. SANS profiles of a) Monarch, b) Herrin, c) Springfield, and d) Blue Gem with Polydisperse Spherical Particle (PDSP) fit indicated by solid red line.

SANS is dependent on the neutron scattering length density (SLD) differences between the solid matrix and the surrounding medium. In the present study, the external medium is made of pores filled with air, imparting them with high neutron contrast in comparison to the coal matrix [44, 46], which is useful to differentiate open and closed pores via contrast matching (CM). The calculated SLDs of the coal matrices, using Eq. (3), and He densities (d in Eq. (3)) are listed in Table 1.

$$\rho_n = \frac{N_A d}{M} \sum_j p_j \left(\sum_i s_i b_i\right)_j \tag{3}$$

The terms in Eq. (3) are as follows: N_A is Avogadro's constant, s_i is the proportion of the number of nucleus i in compound j, p_j is the proportion of the molecular number of the compound j in the mixture, and b_i is the coherent scattering amplitude for nucleus. For these calculations the elemental compositions (C, H, N, S and O) derived from the ultimate analysis (not presented here) were used.

Mixtures of distilled D_2O and H_2O in different ratios were used to match the calculated SLDs of the bituminous coals (Herrin, Springfield and Blue Gem). It was later recognized that the wrong D_2O/H_2O mixture was used for the subbituminous Monarch coal and therefore, the results from this coal are omitted. The SANS patterns of the dry and contrast matched states of these coals are presented in Figure 3.

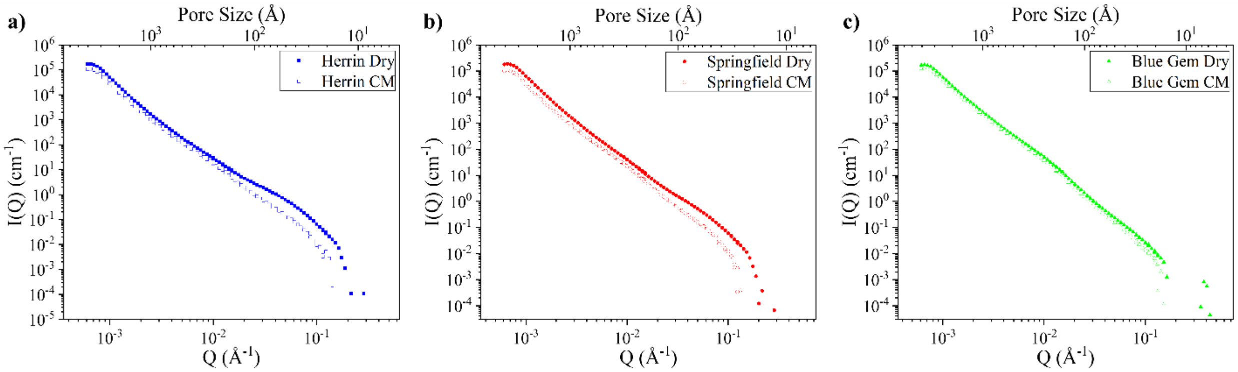

Figure 3. SANS profiles of a) Herrin b) Springfield and c) Blue Gem coals at dry and contrast matched (CM) states.

SANS profiles at contrast match condition show reduced intensity in Herrin and Springfield coals in comparison to their dry states. However, the difference is less significant for Blue Gem coal. This lower difference between the dry and contrast matched conditions in Blue Gem suggests that pore network is poorly connected when compared to other two bituminous coals, Herrin and Springfield, making it the less permeable [47, 48].

The pore size distributions deduced from the PDSP fits with volume weighted pore number densities, $r^3f(r)$ [36, 49], as a function of pore radius, r, are shown in Figure 4a. Here, if the number of pores with a certain size, r, is significantly higher in comparison with other size groups, it exhibits a peak on the pore size distribution curve. If the population does not show appreciable high concentrations zones, a shoulder (i.e., still some degree of concentration) or a smooth change will be shown on the distribution curve (i.e., no detectable concentration). However, the lack of peaks does not translate into being pore-free in the given length-scale but rather not having a strong concentration of pores for a given size to form a cluster that shows a peak on the distribution curve.

Table 1. Maceral, rank, and porosity related properties of the coals. The maceral compositions are presented on a mineral-free basis where V: Vitrinite, I: Inertinite and L: Liptinite. The He densities are obtained from as-received coals on a dry-mineral-matter-free (dmmf) basis. The SANS and MIP data are on dry-basis. The SANS porosity covers both open and closed pores. SANS-Fraction Inaccessible corresponds to the percentage of the inaccessible pores within the detected pores. SANS SSA corresponds to the total specific surface area calculated from the SANS measurements with a probe size extrapolated to 4Å covering all the detected pores.

Coal	Maceral Composition – V/I/L (vol%)	Vitrinite Reflectance (R_0,max %)	He Density (g/cm^3)	SLD (10^{-6}/Å^2)	SANS Porosity (%)	SANS-Fraction Inaccessible (%)	SANS SSA (m^2/g)	MIP Porosity (%)
Monarch	90.2/4.5/5.3	0.39±0.02	1.50	2.16	6.60	-	66	1.94
Herrin	91.0/6.6/2.4	0.65±0.03	1.33	2.14	2.67	39	17	1.68
Springfield	88.6/10.2/1.2	0.67±0.03	1.35	2.24	2.44	43	11	1.08
Blue Gem	84.9/6.7/8.4	0.88±0.05	1.36	2.28	1.48	85	6	1.10

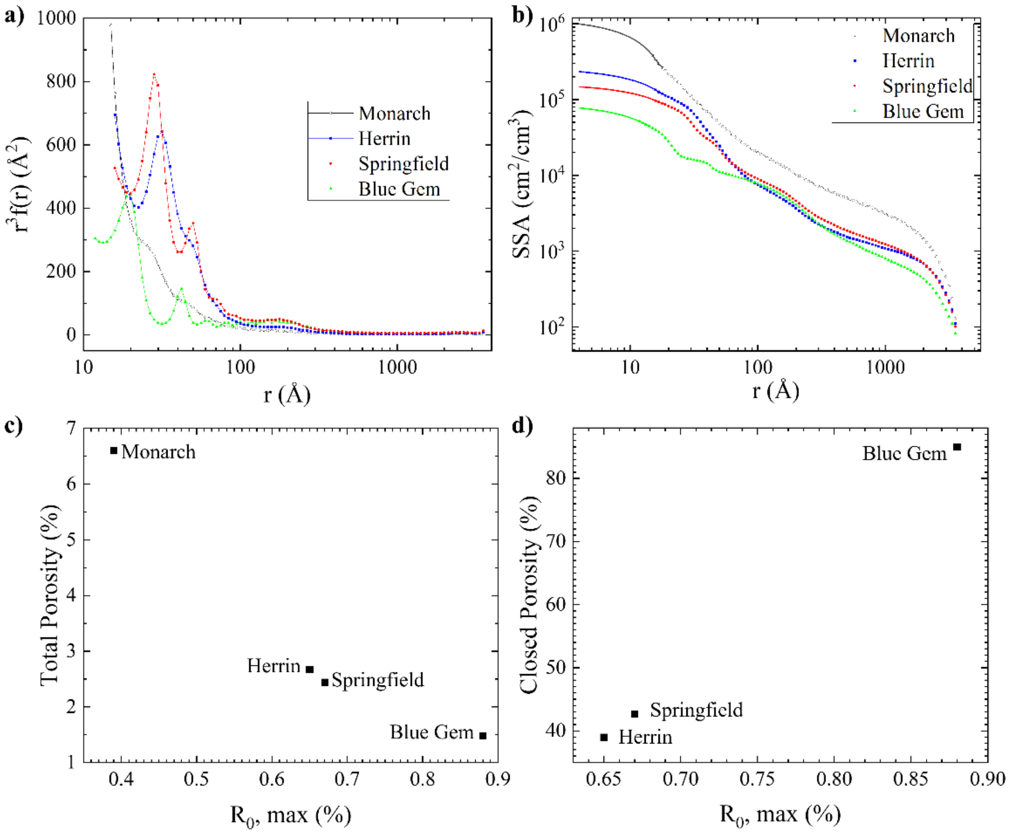

Figure 4. a) Volume-weighted pore number density, $r^3f(r)$, distribution of pores, b) Total Specific Surface Area (SSA) as a function of probe size (size of the hypothetical probing molecule, e.g., probe size of N_2 molecules is 4Å), c) Total porosity – vitrinite reflectance (R_0, max) relation for all the coals, and d) Closed porosity to D_2O/H_2O – vitrinite reflectance (R_0, max) relationship for the bituminous coals.

Figure 4a reveals that all four examined samples have a multi-modal size distribution indicative of hierarchical structures within a mainly mesoporous matrix (bordering microporosity). Particularly the bituminous coals exhibit similar distributions, with Herrin and Springfield coal profiles almost overlapping, while Blue Gem is distinctly separated towards smaller pore sizes. Similar differences in size distribution were previously observed for other bituminous coals where slightly higher maturities were correlated to smaller pores [47].

Meso- and micropores are reported to account for 92-99% of the porosity in bituminous coals [32, 50]. Furthermore, the bituminous coals investigated here are vitrinite-rich and between the various macerals vitrinite is typically more microporous than others [51, 52]. Accordingly, the data presented in Figure 4a agree with the literature for bituminous coals. The subbituminous Monarch coal fails to show distinct peaks while showing shoulders in the otherwise mostly smooth distribution curve. This is also in agreement with the previously reported rank data where the dominant macro- and mesoporosity are higher in low-rank coals [32, 53].

Here the accessible pore size range with SANS is between 10 to 3500 Å (1-350 nm). The modal pore sizes obtained from the peaks and shoulders in Figure 4a are presented in Table 2 in terms of pore radii. Particularly for the Springfield and Blue Gem coals, five different peaks were observed and used as reference points. Accordingly, if a coal did not show a peak for a given Modal r, a value was not presented. Also note that, compared to the rest of the peaks, a significantly broader distribution is observed around Modal r_5, which was only detectable for the bituminous coals.

Table 2. The modal radii from the volume weighted pore size distributions in Figure 4a (dry basis). The values are presented in Å followed by nm in parentheses.

Coal	**Modal r_1**	**Modal r_2**	**Modal r_3**	**Modal r_4**	**Modal r_5**
Monarch	25 (2.5)	47 (4.7)	66 (6.6)	-	-
Herrin	32 (3.2)	50 (5)	70 (7)	-	188 (18.8)
Springfield	28 (2.8)	50 (5)	70 (7)	94 (9.4)	188 (18.8)
Blue Gem	20 (2)	42 (4.2)	63 (6.3)	84 (8.4)	177 (17.7)

Among the bituminous coals, Blue Gem consistently has a pore size distribution skewed towards smaller sizes; an observation in agreement with previous reports. It has been demonstrated that as the rank increases, the observed porosity dominance shifts towards microporosity [19, 32, 51] due to more tightening that occurs in the coal structure making pores increasingly closed with thermally generated bitumen [14, 48]. Figure 4b shows the total specific surface areas (SSA) as a function of the pore (probe) sizes for all the coals including both accessible and inaccessible pores. Here, it must be emphasized that the SSA value for a given probe size (r) in Figure 4b, is a sum of the surface areas of all pores with a radius larger than the probe size divided by the sample volume [36]. Accordingly, the total SSA increases with decreasing pore size (probe size) regardless of the coal rank (right to left in Figure 4b). However, clear differences can be inferred. For example, the subbituminous Monarch coal has a higher SSA value, higher pore surface area and pore volume over the examined size range when compared to the bituminous coals.

Between the three bituminous coals, Herrin and Springfield coals have overlapping SSA curves indicating a similar pore structure and size distribution (Figure 4b). For Blue Gem coal, significantly lower values are observed as the probe size becomes smaller in the <100 Å (10 nm) range. The decrease in SSA with decreasing pore/probe size in this range indicates a reduced microporosity in the Blue Gem coal compared to the other two bituminous coals. The decreasing microporosity with increasing rank in bituminous coals has been well documented [44].

The probe size of SANS for SSA is limited by the instrument resolution. In the current study it is ~10 Å (1 nm). Compared to gas adsorption methods (e.g., N_2 and CO_2) the accessible SSA with SANS remains rather high when compared to a probe size of 4Å (0.4 nm) in the case of N_2 adsorption. The SSA values accessible with smaller probe sizes can be estimated via linear extrapolation of the SANS data (see the solid lines in Figure 4b extending to 4 Å). However, the total SSA calculated via this extrapolation should be regarded at best as a first order approximation with the uncertainty reported to be as high as ±50% [47, 48]. The N_2 adsorption equivalent SSA values are calculated by dividing the SANS SSA values (extrapolated to 4 Å) with the He densities of each coal and are presented in Table 1.

Overall, the SSA values consistently decrease with an increase in rank (Figure 4b and Table 1). All else being equal, a lower SSA would translate into a lower gas adsorption capacity as well as a lower active area for solvents to penetrate and react with the coal.

Vitrinite reflectance (R_0, max) is used as a coal rank indicator with higher values corresponding to higher ranks. Using the vitrinite reflectance values, the total porosities as measured with SANS are presented in Figure 4c as a function of rank. For the coals studied here, a clear correlation between the rank and the total porosity is observed wherein the total porosity decreases with increasing rank. Furthermore, the Herrin and Springfield coals can be seen to be very close in rank accompanied by similar values of total porosity consistent with our findings. Other measurements such as FTIR and NMR have revealed these two coals to have almost the same structure, the results of which will be subject of a future publication. Accordingly, a byproduct of this relation is a validation of the repeatability of the SANS measurements wherein similar coals have revealed similar results.

As the coal rank increases it is also reported that the pore networks become increasingly disconnected, and the inaccessible porosity fraction is expected to increase. As previously stated, the contrast matching SANS data can be used to identify the fraction of the inaccessible (closed) porosity to that fluid. The fractions of the closed pores are presented in Figure 4d as a function of vitrinite reflectance for the bituminous coals. Figure 4d reveals the fraction of closed porosity to increase with increasing rank with the Herrin and Springfield coals again showing similar values.

Previous studies found correlations (at least partial) between: 1) closed pores and inertinite fraction based on pore size and coal origins [18], 2) closed porosity, and vitrinite content [44], 3) pore number densities of various pore sizes and vitrinite reflectance [14], 4) closed porosity and vitrinite reflectance [48]. However, despite the correlation observed in Figure 4d, the dataset was obtained from a very limited set of coals all of which are vitrinite-rich as presented in Section 3.1 (Table 1).

3.3. Mercury intrusion porosimetry

The MIP data from ambient to 346 MPa is presented in Figure 5 as a function of intruded mercury volume for all the studied coals. This dataset will not be used for any quantification because the high pressures needed for these measurements are known to damage/destroy the pore structures due to the soft nature of the coal matrix [54]. Nevertheless, the trends in the data are useful as complementary information to the data already presented.

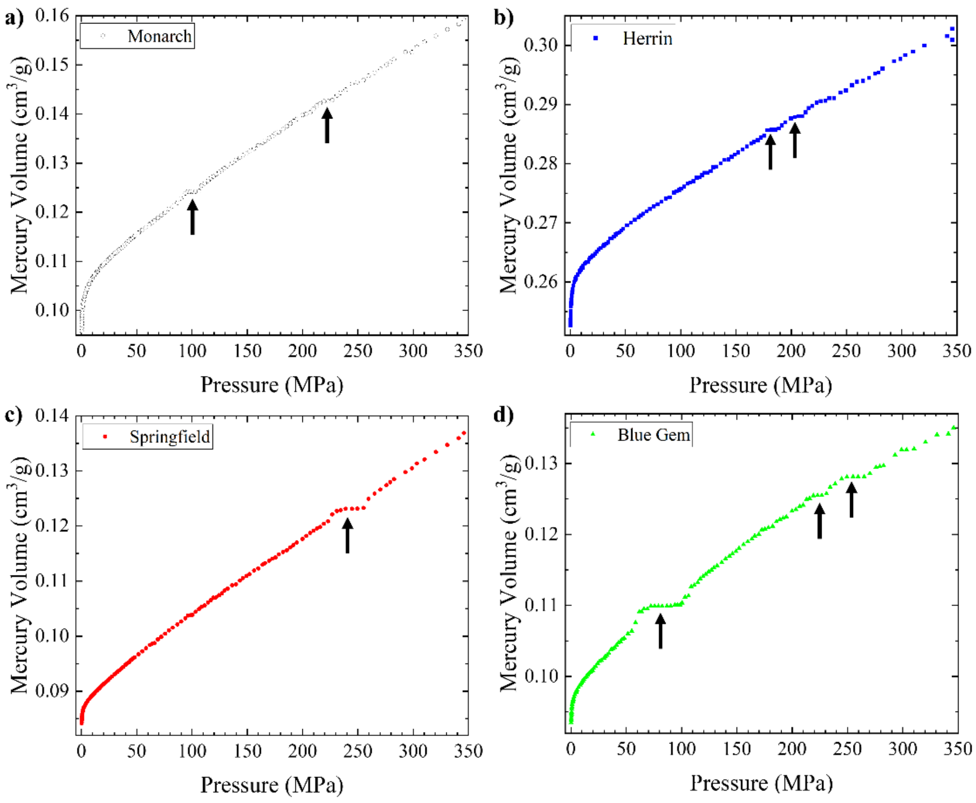

Figure 5. The applied mercury pressure vs intruded mercury volume relation presented up to a total pressure of 346 MPa (50.2 ksi) for: a) Monarch, b) Herrin, c) Springfield, and d) Blue Gem coals. Arrows indicate zones of nearly constant intruded volume despite increasing pressures.

Being an intrusion-based technique, MIP can only detect pores that mercury can infiltrate (i.e., open pores). With increasing pressures, smaller pores can be infiltrated as long as they are connected to the outside via a network. This would result in a mostly linear relation between the applied pressure and intruded mercury volume. However, Figure 5 also shows areas where the intruded volume stays nearly constant despite increasing pressure, as indicated by the arrows on the plots. This is particularly pronounced for the Blue Gem coal where the effect is seen at much lower pressures compared to the rest of the coals.

The information presented in Figure 5 can potentially be used to supplement the SANS results (Figure 4) where resistance to mercury intrusion can be related to the presence of closed pores. Once a critical pressure is overcome then intrusion can continue, as a result of the deformation of the coal matrix and the resulting opening of new pathways.

As stated, this effect is most pronounced in the Blue Gem coal. This is followed by the Springfield and Herrin coals which show similar levels of resistance around similar values of pressures. The Monarch coal, on the other hand, shows little to no resistance to mercury intrusion.

In light of the SANS results (Figure 4c and d), the resistance to mercury penetration follows a similar pattern wherein Springfield and Herrin coals, which have similar amounts of total and closed porosity show similar resistances to mercury intrusion. Blue Gem shows the highest amount of resistance starting from lower pressures in agreement with its significantly lower porosity with highest inaccessibility. While CM SANS data for the Monarch coal was not available to determine inaccessible porosity, the MIP results in Figure 5 can qualitatively suggest the pores to be relatively well-connected with low resistance to mercury intrusion compared to the others. However, the results in Figure 5 remain a qualitative observation and are omitted from further discussion.

For the remainder of this section a maximum mercury pressure of 32 MPa is considered, as explained in Section 2.2, low enough to prevent excessive deformation of the coal matrix. First, the Log(dV/dP)-Log(P) plots are presented in Figure 6 for all the coals within this pressure interval. Plotting the data in this form enables detection of any power law behavior and is typically used to determine the fractal dimension (D) of the coals where the slope of the relation equals D-4 [38, 55].

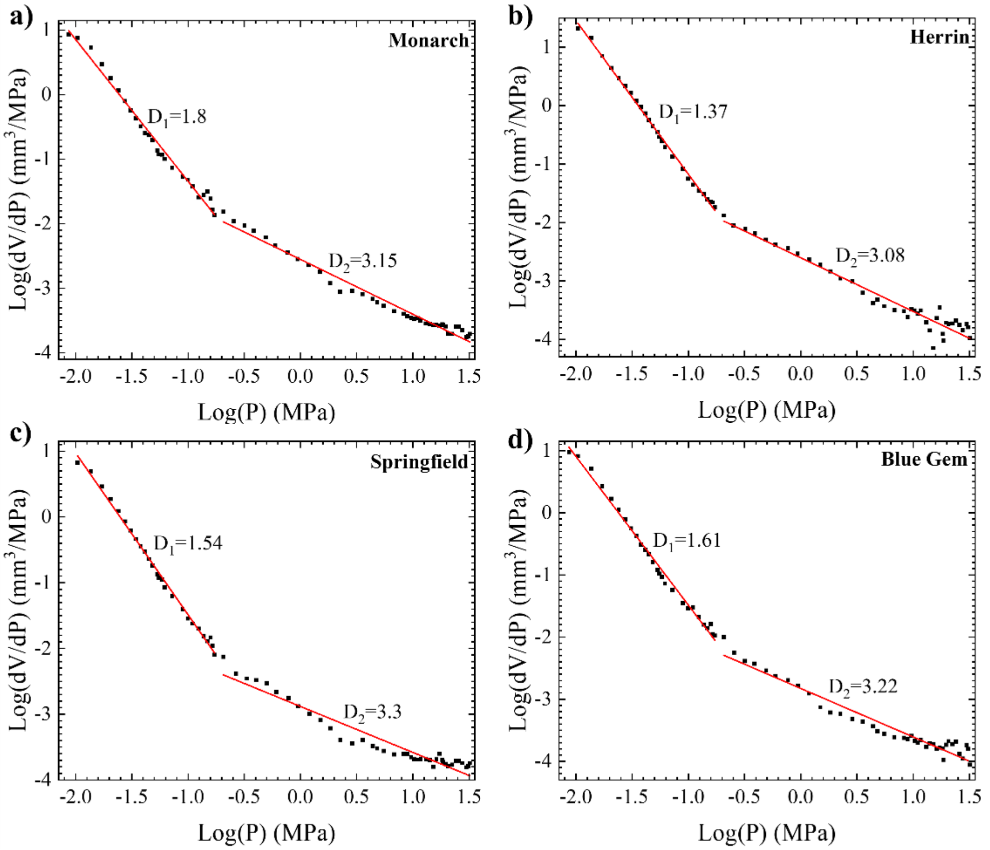

Figure 6. Log(dV/dP)-Log(P) relations for: a) Monarch, b) Herrin, c) Springfield, and d) Blue Gem coals.

The data presented in Figure 6 can be divided into two separate linear regions characterized with two separate slopes yielding fractal dimensions of D_1 and D_2 (values shown on the graphs). The transition between these two regimes happens at a mercury pressure of 0.2 MPa; below and above it is characterized by a fractal dimension of D_1 and D_2, respectively.

As can be seen in Figure 6, for all of the coals $D_1<2$, although the fractal relation for surfaces is expected to be $2<D_s\leq 3$ with $D=2$ indicating perfectly smooth surfaces [38]. In this case, D_1 is regarded as the exponent of a power-law that describes the filling of larger volumes such as surface pores, cracks and interparticle voids at low pressures (<0.2 MPa in this study). As described in Section 2.2 with the relation in Eq. (1), the interparticle voids are expected to be filled at a pressure of 0.2 MPa which coincides with the transition pressure in Figure 6. Accordingly, this region described with D_1 is excluded from further quantification. The region corresponding to P>0.2 MPa is characterized with fractal dimensions, $D_2\approx 3$ indicative of surface features consistent with the SANS results presented in Section 3.1. However, even at these relatively lower pressures the sample is affected by mechanical compression which is manifested in the observed in D_2 values >3 [38].

In Figure 7a, the porosity data for all the coals are presented using the cumulative mercury volume vs. pore radius relation within the pressure range 0.2-32 MPa that corresponds to a pore size range of 3600-23 nm. Here emphasis is placed on the trends rather than the cumulative mercury volume per sample as this metric includes interparticle volume and differences in total material packed inside the measurement bowl.

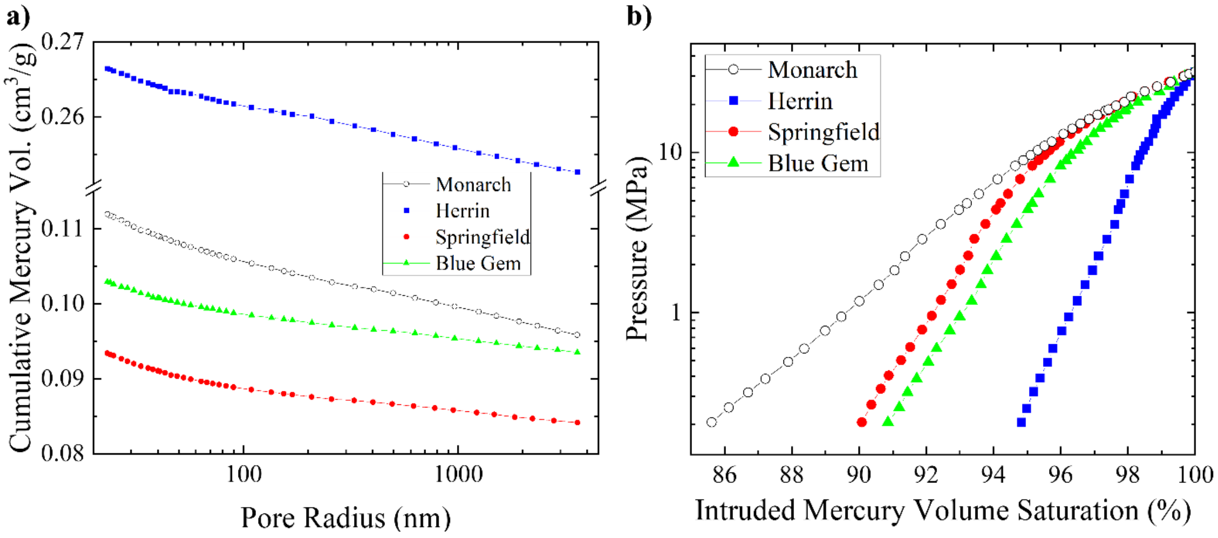

Figure 7. The relation between a) cumulative mercury intrusion (pore) volume and pore radii, and b) the applied mercury injection pressures and the intruded mercury volume saturation.

Data presented in Figure 7a can be divided into two regions of pore radii: 1) r>100 nm and 2) r<100 nm. In agreement with the SANS data, the bituminous coals show similar overall profiles (with Herrin showing slightly steeper slopes) whereas the subbituminous Monarch coal shows clear distinctions in both regions with noticeably steeper slopes. These trends indicate an overall higher porosity in the Monarch coal throughout the whole studied range with the Herrin coal having the highest porosity within the bituminous coals.

The calculated total porosities from MIP measurements (within P=0.2-32 MPa) are listed in Table 1, in comparison to the SANS porosity. Here the MIP porosities are consistently lower than those obtained with SANS because SAS techniques detect both open and closed porosity. Previously reported that results from SANS measurements also indicated higher values of porosity when compared to gas adsorption or MIP data of the same coals [32, 50, 53].

Comparing the porosity data from SANS and MIP (Table 1), the overall trend can be seen to be similar with Monarch having the highest porosity followed by Herrin and Springfield coals. However, the MIP porosity data does not perfectly mimic the trends from SANS data and analysis, particularly for the Blue Gem coal that shows similar amount of total porosity to that of the Springfield coal based on MIP data. Furthermore, the difference in porosity between the Herrin and Springfield coals is more pronounced in the MIP data compared to SANS as shown in Table 1. Naturally, such discrepancies can be expected considering that the two techniques probe different size ranges and MIP is an invasive method that cannot detect closed porosity without excessive deformation (and thus opening the pores). Nevertheless, the MIP dataset is meant to be complementary to SANS data, and the agreement between the two is satisfactory for the purposes of this study.

Finally in Figure 7b, the intrusion pressures are plotted with respect to the intruded mercury volume saturation within the pressure range P=0.2-32 MPa for all the coals. Here, the slopes of the relations point to the level of pore connectivity where steeper slopes indicate less connected pores (i.e., harder for mercury to penetrate) [30]. In agreement with the data presented, the bituminous coals exhibit similar trends whereas the subbituminous Monarch coal shows a noticeably more gradual slope. A more gradual slope would normally indicate the presence of cracks and macropores [56]. However, within the investigated pressures, the filling of cracks and large surface pores should have been accounted for by the lower pressure limit (and omitted here). Instead, the pore network of the Monarch coal can be concluded to be better connected compared to the bituminous coals studied here.

3.4. N_2 gas adsorption

The low pressure N_2 adsorption/desorption isotherms of the four coal samples are shown in Figure 8. Monarch and Springfield isotherms (Figure 8a and Figure 8c) are of type IV, with a hysteresis loop representing the mesoporous nature of these samples [32, 47, 57]. The shape of the hysteresis loops are of type H3 [57] which is associated with the presence of slit-shaped pores that lead to capillary condensation and delayed desorption [58, 59]. The larger hysteresis observed in Monarch coal could be related to higher pore accessibility and therefore leading to higher gas adsorption and delayed desorption [47]. Herrin coal also shows the presence of a hysteresis loop (Figure 8b) however, significantly less defined in comparison suggesting the least amount of interconnectivity between these three coals.

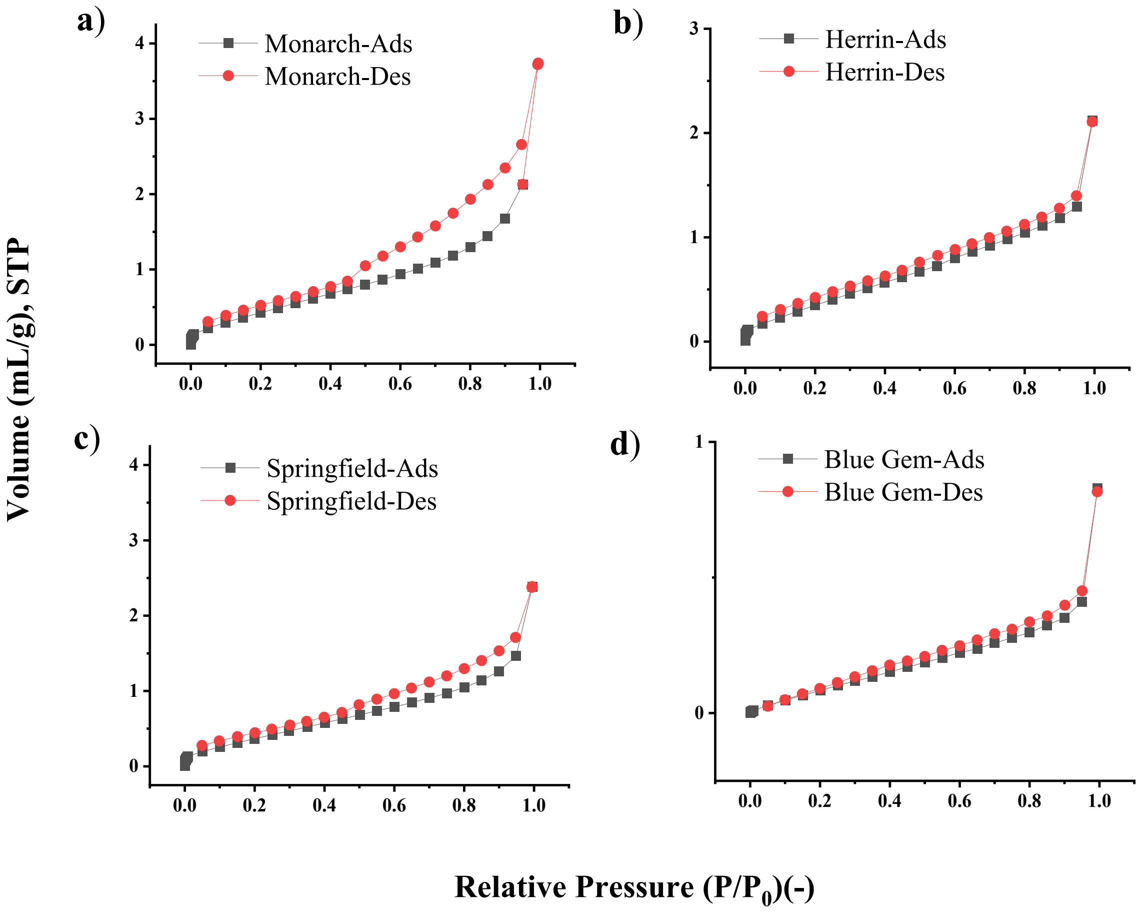

Figure 8. N_2 adsorption/desorption isotherms of a) Monarch b) Herrin c) Springfield and d) Blue Gem coal samples.

On the other hand, the Blue Gem coal shows a reversible type II (Figure 8d) isotherm based on the IUAPC classification [57]. This type of isotherm is stated to correspond to either a non-porous or a macroporous solid wherein the adsorption/desorption occurs unrestricted (or does not occur in case of non-porous solids).

This observation of low porosity of Blue Gem is in agreement with the SANS results presented in Section 3.2. To elaborate, the N_2 molecules are unable to access the pore structure of the Blue Gem coal as evidenced by the lowest amount of N_2 adsorption. Not surprisingly, the Blue Gem coal is found to have the smallest surface area accessible to N_2 molecules (Table 3), with more details below.

The surface areas of the four coals were calculated using Brunauer-Emmett-Teller (BET), Barrett-Joyner-Halenda (BJH), and Density Functional Theory (DFT) methods and are presented in Table 3. The results are well-aligned between the three different interpretation methods and show that the subbituminous Monarch coal possesses the highest pore surface area, in agreement with the interpretation of the adsorption/desorption curves shown in Figure 8. Surface area for bituminous Herrin and Springfield coals are closely aligned which is in turn, consistent with the results obtained from SANS and MIP. Finally, Blue Gem coal has the smallest surface area (3-5 times lower than the other coals studied), again consistent with the previously presented results.

While the SSA values obtained from SANS and N_2 adsorption are significantly different (with SANS data being much higher), the overall trends noted are in good agreement. This observation is in agreement as well with previous studies, in particular how N_2 adsorption underestimates the SSA and porosity compared to other techniques and can only detect open pores [32]. Furthermore, as explained in Section 3.1, SANS derived SSA values can only serve as a first approximation. Therefore, the agreement between the two datasets is satisfactory for the purposes of this work.

Table 3. Low pressure N_2 adsorption results of the Monarch, Herrin, Springfield and Blue Gem coals obtained on dry-basis. Note that the calculated pore sizes correspond to the pore openings and not necessarily the actual diameters of the pores.

Coals	BET surface area (m^2/g)	BJH desorption surface area (m^2/g)	DFT cumulative surface area (m^2/g)	BJH desorption pore volume $x10^{-2}$ (cc/g)	DFT cumulative pore volume $x10^{-2}$ (cc/g)	BJH desorption pore diameter Ǻ (nm)	DFT pore diameter Ǻ (nm)
Monarch	2.01	2.46	1.61	0.59	0.44	38 (3.8)	34 (3.4)
Herrin	1.70	1.20	1.15	0.29	0.24	38 (3.8)	20 (2)
Springfield	1.5	1.36	1.25	0.34	0.28	38 (3.8)	34 (3.4)
Blue Gem	0.48	0.33	0.30	0.12	0.08	43 (4.3)	26 (2.6)

The cumulative pore volumes and pore size distributions as a function of average pore width (pore opening) are shown in Figure 9 BJH (top row) and DFT (bottom row).

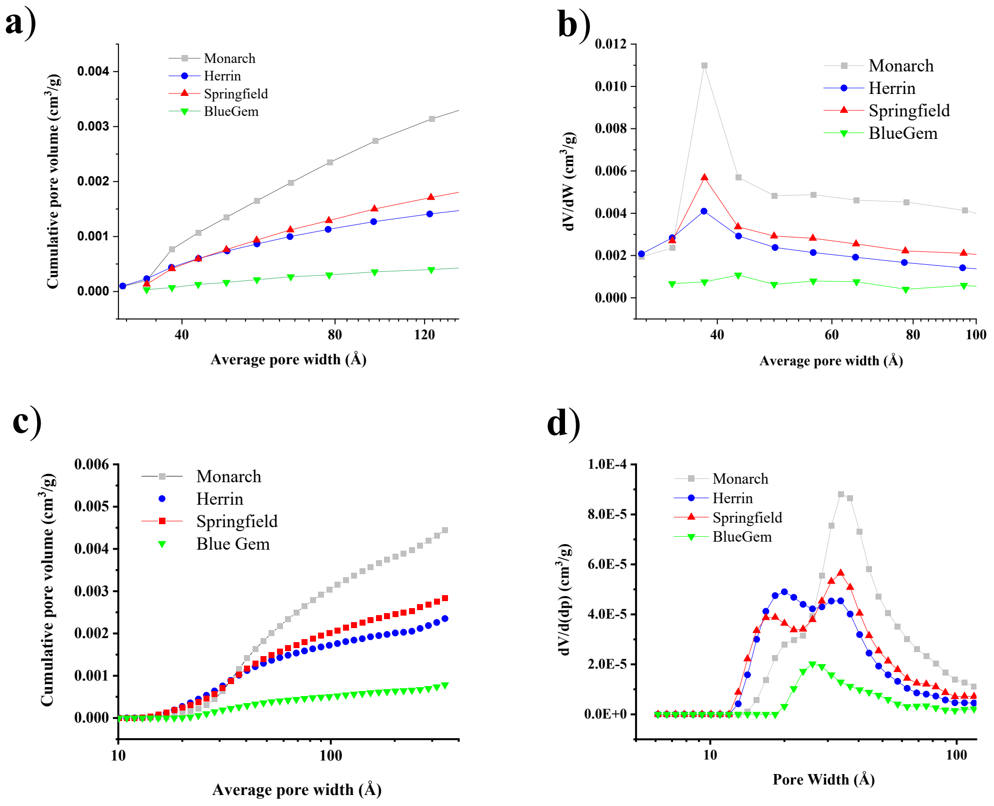

Figure 9. Pore volume distribution curves of coal samples from N_2 adsorption isotherms using BJH (a, b) and DFT (c, d) models.

Figure 9 shows that the DFT model provides better granularity and hence better data resolution in comparison to the BJH model. This is because DFT is a newer method where pore volumes and pore size distributions are calculated from adsorption potentials while BJH model relies on capillary theories. Regardless, both models reveal similar trends among the investigated coals.

Both Figures 9a and 9c show the cumulative pore volumes follow the order of Monarch, Springfield, Herrin and Blue Gem from highest to lowest, with the Herrin and Springfield coals being close in value in agreement with the previous results. In agreement with the MIP data (Figure 7), the Monarch coal shows steeper slopes suggesting easier uptake of N_2 and thus, easier pore accessibility which is in contrast to the behavior of Blue Gem coal, consistent with the difficulty to access pore structure.

The pore size distributions from the BJH and DFT models are presented in Figures 9b and 9d, respectively. Similar to the dataset presented in Figure 4a, peaks are observed when pore clusters are formed within a given size range. Here, it must be emphasized that the DFT derived size distribution offers a better resolution, presenting additional concentration zones in the form of shoulders, i.e., a multimodal distribution similar to the SANS data presented earlier.

Following the continuity between the techniques, the Herrin and Springfield coals show almost overlapping profiles (Figure 9d). Different from the SANS data, the Blue Gem coal shows a distribution that is slightly shifted to larger sizes compared to the other bituminous coals. While this would appear as a discrepancy at first, it could actually be related to a fraction of the pores being inaccessible to N_2 adsorption (i.e., closed porosity in agreement with SANS); effectively skewing the pore size distribution.

Finally, the pore diameters (for pore openings) obtained from the strongest peaks (i.e., highest concentrations) are presented in Table 3 for all the coals from both the BJH and DFT techniques. The pore sizes inferred from N_2 adsorption, corresponding to the largest concentrations (Table 3), agree well with the pore size distributions from the SANS measurements, Table 2 (again, note that SANS data represent pore radii whereas N_2 adsorption shows diameters of the pore openings in addition to being limited to open pores).

Overall, the porosity and pore accessibility of the coals studied here with three different techniques revealed consistent results where each technique offered complimentary information with decent overlap. All else being equal, theoretically the porosity data would suggest the Monarch coal to be more easily accessible to react with chemical reagents whereas the Blue Gem would be the hardest. The Herrin and Springfield coals would be in between these two and show similar characteristics to one another.

However, as stated earlier, coal porosity and its size distribution are only first approximations for extractability. This is because coal is a highly heterogeneous material with both inorganic and organic phases that can greatly affect the solvent extraction processes. Furthermore, the type of extractable molecules depends on the coal precursor which eventually affects the end-product. Accordingly, following measurements of porosity and pore accessibility systematic studies with solvents would be required to find a reliable correlation between solvent penetration, porosity/pore accessibility of the coals as well as useful end-products.

4. Summary and conclusions

In this work, the porosity and pore accessibility of three bituminous coals (Herrin, Springfield, and Blue Gem) and one subbituminous coal (Monarch) were investigated using small angle neutron scattering (SANS), mercury intrusion porosimetry (MIP) and low pressure N_2 adsorption techniques. The SANS measurements were performed in both as-received and contrast-matched conditions where a contrast-matching D_2O/H_2O mixture infiltrates and blocks signal from open pores.

The investigated coals were all vitrinite-rich and ranked from low to high as Monarch, Herrin, Springfield and Blue Gem based on vitrinite reflectance (R_0, max) values of 0.39, 0.65, 0.67, and 0.88%, respectively.

Based on the SANS data, the highest porosity (open+closed) was observed in the Monarch coal followed by Herrin and Springfield (close in value), and Blue Gem coals. The decreasing porosity from Monarch to Blue Gem was found to agree with the increase in coal rank where increased maturity leads to tightening of the macerals. Inaccessible porosity follows an opposite trend, with Blue Gem coal found to have the highest amount of inaccessible porosity followed by Springfield and Herrin coals. This also showed a good correlation with rank where the fraction of inaccessible pores increased with increasing rank, for the coals studied here. However, the data cannot be generalized to other coals as the coals studied here constitute a highly limited set all of which were vitrinite-rich.

The pore size distributions obtained from the SANS measurements revealed the pores to be concentrated in the mesopore range with similar size distributions albeit still related to rank where smaller pores could be observed with increasing rank. This was again related to the tightening of the macerals over geological time with increased maturity. The specific surface area (SSA) values were also calculated from the SANS results and found also to be correlated to coal rank with the lowest SSA in Blue Gem and highest SSA in Monarch where the SSA is expected to increase with increased porosity.

Complementary MIP and N_2 adsorption measurements were also conducted to further understand the pore structure of the four coals. With MIP, similar trends in total porosities were observed, where it was shown that Blue Gem coal had lower pore accessibility with the smallest amount of pore volume while Monarch coal had the most accessible pore network with the highest amount of pores.

The adsorption/desorption data from the N_2 adsorption measurements also revealed a more accessible pore structure for the Monarch coal and a closer to a non-porous nature of Blue Gem coal in agreement with its high fraction of inaccessible porosity. The total pore volumes and SSA values in relation to the coal rank were found to qualitatively agree with the SANS data. Deviations in quantification between the different techniques is expected due to the different probing methods as well as SANS being able to detect both closed and open pores. Therefore, the agreement in the observed trends between the different techniques was satisfactory for the purposes of this work. Finally, the pore size distributions were also found to agree with the SANS results.

Acknowledgements

This research work was sponsored by the U.S. Department of Energy Fossil Energy and Carbon Management Program, Advanced Coal Processing Program, C4WARD project (FEAA155). This research used resources at the High Flux Isotope Reactor, a DOE Office of Science User Facility operated by the Oak Ridge National Laboratory. The critical review of Dr. Thomas R. Watkins is greatly appreciated.

References

[1] C. Song, H.H. Schobert, Opportunities for developing specialty chemicals and advanced materials from coals, Fuel Process Technol 34(2) (1993) 157-196.

[2] H.H. Schobert, C. Song, Chemicals and materials from coal in the 21st century, Fuel 81(1) (2002) 15-32.

[3] J.M. Andrésen, C.E. Burgess, P.J. Pappano, H.H. Schobert, New directions for non-fuel uses of anthracites, Fuel Process Technol 85 (2004) 1373-1392.

[4] S.R. Isabel, C.C. John, Coal-derived carbon materials, in: S.R. Isabel, C.C. John (Eds.), Applied coal petrology, Elsevier, Burlington, 2008, pp. 193-225.

[5] V.C. Hoang, M. Hassan, V.G. Gomes, Coal derived carbon nanomaterials - recent advances in synthesis and applications, Appl Mater Today 12 (2018) 342-358.

[6] Y.A. Al-Majali, C.T. Chirume, E.P. Marcum, D.A. Daramola, K.S. Kappagantula, J.P. Trembly, Coal-filler-based thermoplastic composites as construction materials: A new sustainable end-use application, ACS Sustain Chem Eng 7(19) (2019) 16870-16878.

[7] National Coal Council, Coal in the New Carbon Age. https://www.nationalcoalcouncil.org, 2019.

[8] I. Reid, Advances in non-energy products from coal, IEA Clean Coal Centre, 2021, pp. 1-90.

[9] A.H. Hamdani, X-ray computed tomography analysis of sajau coal, Berau Basin, Indonesia: 3D imaging of cleat and microcleat characteristics, Int J Geophys 2015 (2015).

[10] S. Dai, R.B. Finkelman, D. French, J.C. Hower, I.T. Graham, F. Zhao, Modes of occurrence of elements in coal: A critical evaluation, Earth-Sci Rev 222 (2021) 103815.

[11] J.P. Mathews, Q.P. Campbell, H. Xu, P. Halleck, A review of the application of x-ray computed tomography to the study of coal, Fuel 209 (2017) 10-24.

[12] S. Mazumder, K.-H. Wolf, K. Elewaut, R. Ephraim, Application of x-ray computed tomography for analyzing cleat spacing and cleat aperture in coal samples, Int J Coal Geol 68(3-4) (2006) 205-222.

[13] M. Van Geet, R. Swennen, Quantitative 3D-fracture analysis by means of microfocus x-Ray Computer Tomography (μCT): An example from coal, Geophys Res Lett 28(17) (2001) 3333-3336.

[14] A. Radlinski, M. Mastalerz, A. Hinde, M. Hainbuchner, H. Rauch, M. Baron, J. Lin, L. Fan, P. Thiyagarajan, Application of SAXS and SANS in evaluation of porosity, pore size distribution and surface area of coal, Int J Coal Geol 59(3-4) (2004) 245-271.

[15] J. Rouquerol, D. Avnir, C. Fairbridge, D. Everett, J. Haynes, N. Pernicone, J. Ramsay, K. Sing, K. Unger, Recommendations for the characterization of porous solids (Technical Report), Pure Appl Chem 66(8) (1994) 1739-1758.

[16] J.S. Gethner, The determination of the void structure of microporous coals by small-angle neutron scattering: Void geometry and structure in Illinois No. 6 bituminous coal, J Appl Phys 59(4) (1986) 1068-1085.

[17] Y.B. Melnichenko, L. He, R. Sakurovs, A.L. Kholodenko, T. Blach, M. Mastalerz, A.P. Radliński, G. Cheng, D.F. Mildner, Accessibility of pores in coal to methane and carbon dioxide, Fuel 91(1) (2012) 200-208.

[18] R. Sakurovs, L. Koval, M. Grigore, A. Sokolova, L.F. Ruppert, Y.B. Melnichenko, Nanometre-sized pores in coal: Variations between coal basins and coal origin, Int J Coal Geol 186 (2018) 126-134.

[19] H. Gan, S. Nandi, P. Walker Jr, Nature of the porosity in American coals, Fuel 51(4) (1972) 272-277.

[20] Y.X. Zhao, S.M. Liu, D. Elsworth, Y.D. Jiang, J. Zhu, Pore structure characterization of coal by synchrotron small-angle x-ray scattering and transmission electron microscopy, Energ Fuels 28(6) (2014) 3704-3711.

[21] L. Cartz, P.B. Hirsch, A contribution to the structure of coals from x-ray diffraction studies, Phil. Trans. Roy. Soc., Series A, Math Phys Sci A252 (1960) 557.

[22] M. Mastalerz, A. Drobniak, R. Walker, D. Morse, Coal lithotypes before and after saturation with CO_2; insights from micro- and mesoporosity, fluidity, and functional group distribution, Int J Coal Geol 83(4) (2010) 467-474.

[23] L.J. Pyrak-Nolte, C.D. Montemagno, D.D. Nolte, Volumetric imaging of aperture distributions in connected fracture networks, Geophys Res Lett 24(18) (1997).

[24] J.D.N. Pone, P.M. Halleck, J.P. Mathews, Sorption capacity and sorption kinetic measurements of CO_2 and CH_4 in confined and unconfined bituminous coal, Energ Fuels 23(9) (2009) 4688-4695.

[25] S. Hol, C.J. Peach, C.J. Spiers, Applied stress reduces the CO_2 sorption capacity of coal, Int J Coal Geol 85(1) (2011) 128-142.

[26] L.T. Mao, N. Hao, L.Q. An, F.P. Chiang, H.B. Liu, 3D mapping of carbon dioxide-induced strain in coal using digital volumetric speckle photography technique and x-ray computer tomography, Int J Coal Geol 147 (2015) 115-125.

[27] J.D.N. Pone, P.M. Halleck, J.P. Mathews, 3D characterization of strains in coal induced by compression, carbon dioxide sorption, and desorption at in situ stress conditions, Int J Coal Geol 82(3-4) (2010) 262-268.

[28] C. Peng, C. Zou, Y. Yang, G. Zhang, W. Wang, Fractal analysis of high rank coal from southeast Qinshui basin by using gas adsorption and mercury porosimetry, J Petrol Sci Eng 156 (2017) 235-249.

[29] Y. Li, D. Song, S. Liu, X. Ji, H. Hao, Evaluation of pore properties in coal through compressibility correction based on mercury intrusion porosimetry: A practical approach, Fuel 291 (2021) 120130.

[30] Y. Yao, D. Liu, Comparison of low-field NMR and mercury intrusion porosimetry in characterizing pore size distributions of coals, Fuel 95 (2012) 152-158.

[31] R. Sakurovs, A.P. Radlinski, Y.B. Melnichenko, T. Blach, G. Cheng, H. Lemmel, H. Rauch, Stability of the bituminous coal microstructure upon exposure to high pressures of helium, Energ Fuel 23(10) (2009) 5022-5026.

[32] G.N. Okolo, R.C. Everson, H.W. Neomagus, M.J. Roberts, R. Sakurovs, Comparing the porosity and surface areas of coal as measured by gas adsorption, mercury intrusion and SAXS techniques, Fuel 141 (2015) 293-304.

[33] W.T. Heller, M. Cuneo, L. Debeer-Schmitt, C. Do, L. He, L. Heroux, K. Littrell, S.V. Pingali, S. Qian, C. Stanley, The suite of small-angle neutron scattering instruments at Oak Ridge National Laboratory, J Appl Crystallogr 51(2) (2018) 242-248.

[34] W.T. Heller, J. Hetrick, J. Bilheux, J.M.B. Calvo, W.R. Chen, L. DeBeer-Schmitt, C. Do, M. Doucet, M.R. Fitzsimmons, W.F. Godoy, DRTSANS: The data reduction toolkit for small-angle neutron scattering at Oak Ridge National Laboratory, SoftwareX 19 (2022) 101101.

[35] A.P. Radlinski, Small-angle neutron scattering and the microstructure of rocks, Rev Mineral Geochem 63(1) (2006) 363-397.

[36] A.L. Hinde, PRINSAS–a Windows-based computer program for the processing and interpretation of small-angle scattering data tailored to the analysis of sedimentary rocks, J Appl Crystallogr 37(6) (2004) 1020-1024.

[37] D. Smith, S. Schentrup, Mercury porosimetry of fine particles: Particle interaction and compression effects, Powder Technol 49(3) (1987) 241-247.

[38] W. Friesen, R. Mikulla, Mercury porosimetry of coals, Fuel 67(11) (1988).

[39] Y. Yao, D. Liu, D. Tang, S. Tang, W. Huang, Z. Liu, Y. Che, Fractal characterization of seepage-pores of coals from China: an investigation on permeability of coals, Comput Geosci 35(6) (2009) 1159-1166.

[40] E. Cakmak, J.C. Hower, J.P. Mathews, M.C. Weisenberger, R. Kaplan, J. Lacy, Y. Wang, E. Lara-Curzio, Microstructural characterization of three bituminous Illinois Basin coals and a subbituminous Powder River Basin Coal as raw material candidates for carbon fiber precursor production, *in preparation,* 2023.

[41] A. Radliński, C. Boreham, P. Lindner, O. Randl, G. Wignall, A. Hinde, J. Hope, Small angle neutron scattering signature of oil generation in artificially and naturally matured hydrocarbon source rocks, Org Geochem 31(1) (2000) 1-14.

[42] A.P. Radlinski, T.L. Busbridge, E.M. Gray, T.P. Blach, G. Cheng, Y.B. Melnichenko, D.J. Cookson, M. Mastalerz, J. Esterle, Dynamic micromapping of CO_2 sorption in coal, Langmuir 25(4) (2009) 2385-2389.

[43] H.D. Bale, P.W. Schmidt, Small-angle x-ray-scattering investigation of submicroscopic porosity with fractal properties, Phys Rev Lett 53(6) (1984) 596.

[44] R. Sakurovs, L. He, Y.B. Melnichenko, A.P. Radlinski, T. Blach, H. Lemmel, D.F. Mildner, Pore size distribution and accessible pore size distribution in bituminous coals, Int J Coal Geol 100 (2012) 51-64.

[45] A. Radlinski, C. Boreham, G. Wignall, J.-S. Lin, Microstructural evolution of source rocks during hydrocarbon generation: a small-angle-scattering study, Phys Rev B 53(21) (1996) 14152.

[46] Y. Melnichenko, A. Radlinski, M. Mastalerz, G. Cheng, J. Rupp, Characterization of the CO_2 fluid adsorption in coal as a function of pressure using neutron scattering techniques (SANS and USANS), Int J Coal Geol 77(1-2) (2009) 69-79.

[47] M. Mastalerz, L. He, Y.B. Melnichenko, J.A. Rupp, Porosity of coal and shale: Insights from gas adsorption and SANS/USANS techniques, Energ Fuel 26(8) (2012) 5109-5120.

[48] L. He, Y.B. Melnichenko, M. Mastalerz, R. Sakurovs, A.P. Radlinski, T. Blach, Pore accessibility by methane and carbon dioxide in coal as determined by neutron scattering, Energ Fuel 26(3) (2012) 1975-1983.

[49] M. Tricker, A. Grint, G. Audley, S. Church, V. Rainey, C. Wright, Application of small-angle neutron scattering (SANS) to the study of coal porosity, Fuel 62(9) (1983) 1092-1096.

[50] Z. Spitzer, Mercury porosimetry and its application to the analysis of coal pore structure, Powder Technol 29(1) (1981) 177-186.

[51] P.J. Crosdale, B.B. Beamish, M. Valix, Coalbed methane sorption related to coal composition, Int J Coal Geol 35(1-4) (1998) 147-158.

[52] G.R. Chalmers, R.M. Bustin, On the effects of petrographic composition on coalbed methane sorption, Int J Coal Geol 69(4) (2007) 288-304.

[53] R. Zhang, S. Liu, J. Bahadur, D. Elsworth, Y. Melnichenko, L. He, Y. Wang, Estimation and modeling of coal pore accessibility using small angle neutron scattering, Fuel 161 (2015) 323-332.

[54] Z. Li, D. Liu, Y. Cai, G. Si, Y. Wang, Pore structure and compressibility characteristics of heat-treated coals by N_2 adsorption/desorption and mercury intrusion porosimetry, Energ Fuel 34(3) (2020) 3173-3187.

[55] W. Friesen, O. Ogunsola, Mercury porosimetry of upgraded western Canadian coals, Fuel 74(4) (1995) 604-609.

[56] X. Li, Y. Kang, M. Haghighi, Investigation of pore size distributions of coals with different structures by nuclear magnetic resonance (NMR) and mercury intrusion porosimetry (MIP), Measurement 116 (2018) 122-128.

[57] M. Thommes, K. Kaneko, A.V. Neimark, J.P. Olivier, F. Rodriguez-Reinoso, J. Rouquerol, K.S. Sing, Physisorption of gases, with special reference to the evaluation of surface area and pore size distribution (IUPAC Technical Report), Pure Appl Chem 87(9-10) (2015) 1051-1069.

[58] Z. Wang, Y. Cheng, K. Zhang, C. Hao, L. Wang, W. Li, B. Hu, Characteristics of microscopic pore structure and fractal dimension of bituminous coal by cyclic gas adsorption/desorption: An experimental study, Fuel 232 (2018) 495-505.

[59] W. Han, G. Zhou, D. Gao, Z. Zhang, Z. Wei, H. Wang, H. Yang, Experimental analysis of the pore structure and fractal characteristics of different metamorphic coal based on mercury intrusion-nitrogen adsorption porosimetry, Powder Technol 362 (2020) 386-398.

TOC Figure

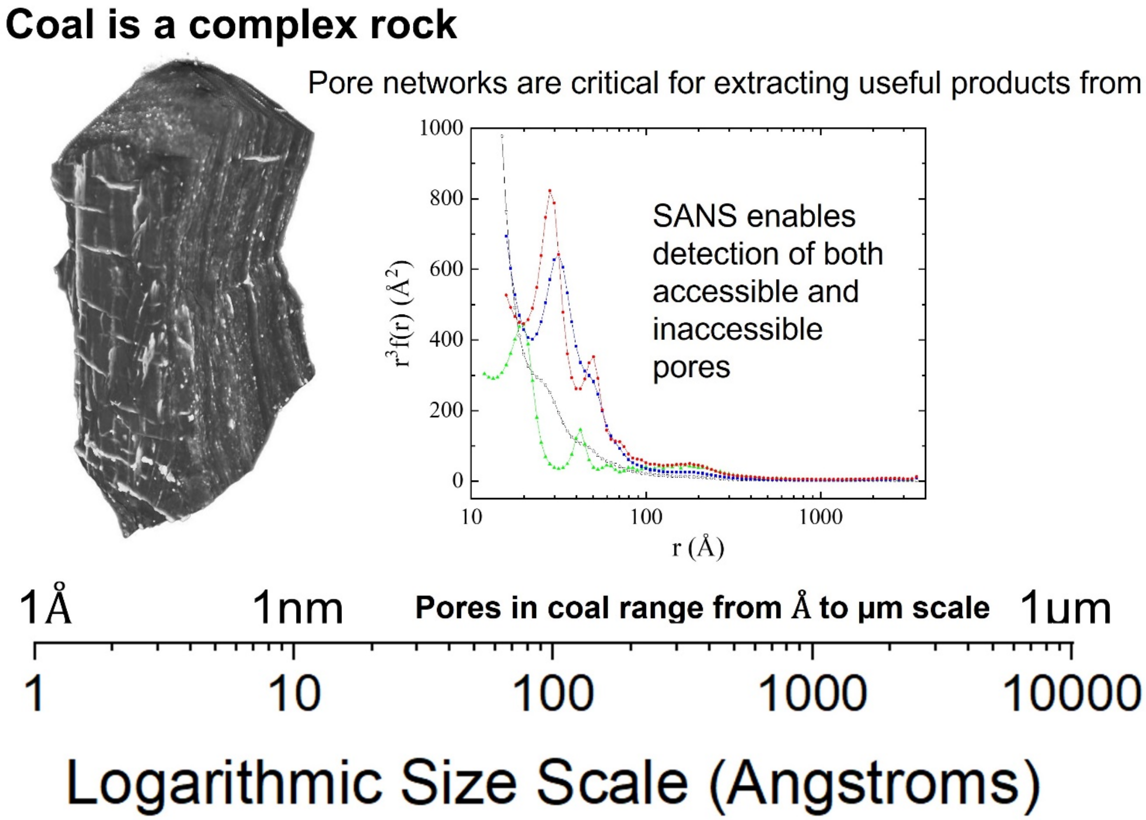
Coal is a complex rock
Pore networks are critical for extracting useful products from coal
SANS enables detection of both accessible and inaccessible pores
1000
800
600
400
200
0
r³f(r) (Å²)
10
100
1000
r (Å)
1Å
1nm
Pores in coal range from Å to μm scale
1um
1
10
100
1000
10000
Logarithmic Size Scale (Angstroms)